Research Article | Vol. 10, No. 10 / 1 October 2020 / Optical Materials Express 2406

Optical Materials EXPRESS

High-birefringence waveguide Bragg gratings fabricated in a silica-on-silicon platform with displacement Talbot lithography

XI-CHEN LUO,[1,2] CHAO CHEN,[1,2,*] LI QIN,[1] XING ZHANG,[1] YONG-YI CHEN,[1] BIAO WANG,[1] LEI LIANG,[1] PENG JIA,[1] YONG-QIANG NING,[1] AND LI-JUN WANG[1]

[1] *State Key Laboratory of Luminescence and Application, Changchun Institute of Optics, Fine Mechanics and Physics, Chinese Academy of Sciences, Changchun 130033, China*
[2] *Center of Materials Science and Optoelectronics Engineering, University of Chinese Academy of Sciences, Beijing 100049, China*
[*] *chenc@ciomp.ac.cn*

Abstract: High-birefringence waveguide Bragg gratings for the C-band are fabricated in the Silica-on-Silicon platform with Displacement Talbot Lithography (DTL). Transmission and reflection spectrums of the Bragg wavelength splitting were measured and calculated. The birefringence here is up to 7.919×10^{-4} to 1.670×10^{-3}, much higher than existing devices via other platforms. We illustrate the principle and advantage of DTL though theoretical analysis and numerical simulation. The birefringence of waveguide Bragg gratings here are customized with their device configuration (i.e., waveguide width and grating etched depth), enabling an effective method to construct scalable Silica-on-Silicon devices for highly linear-polarized external-cavity semiconductor lasers.

1. Introduction

High birefringence photonic devices are key elements for polarization-sensitive optical systems, such as polarizers, polarization beam splitters and wave plates [1–4]. In particular, high-birefringence waveguide Bragg gratings (WBG) have good potential in constructing highly linear-polarized external cavity semiconductor lasers (ECSLs) [5–7]. While a stable linearly polarized laser output is usually achieved by a polarization controller in the optical system, it complicates the system and increases the loss [8]. Therefore, as an external reflector with a selected polarization mode, high-birefringence WBG can be used to cost-efficiently fabricate linearly polarized compact lasers. Meanwhile, the higher birefringence of WBG facilitates the realization of on-chip ECSL, since these planar WBGs are easy to monolithically integrate with laser diodes. One of the significant ECSL's performance is the polarization-extinction ratio (PER), which directly depends on the birefringence of WBG.

However, there are two major challenges in the study of high birefringence WBG. One is the birefringence of WBG is not high enough, so that series of work focus on birefringence suppression [9]. For example, Belaid Tabti *et al*. fabricated polarization-insensitive WBG in Si_3N_4, the birefringence value of which was 4.48×10^{-4} [10]; Luis A. Fernandes *et al*. fabricated WBG in fused silica by femtosecond laser exposure with a maximum birefringence value of 4.35×10^{-4} [3]; the birefringence value of polymer WBG reported by Nam-Seon Son *et al*. was 1.34×10^{-3} [11]. The performance of all the WBGs above is inadequate to meet the need of ECSL with high PER. The other issue is the resolution of the grating pattern linewidth generally in the range of hundreds of nanometers for Silica-on-Silicon, Silicon-on-Insulator or other frequently-used waveguide materials, while the periodic patterns need to be constructed in a large area at relatively low cost [12–14]. Projection optical lithography has been applied for the

#402937 https://doi.org/10.1364/OME.402937
Journal © 2020 Received 15 Jul 2020; revised 18 Aug 2020; accepted 19 Aug 2020; published 2 Sep 2020

Optical Materials EXPRESS

fabrication for micro/nano-electronics [15], but the limited focusing depth and high cost hinder its wide application. Laser-direct-writing technologies can induce birefringence flexibly by adjusting the processing parameters like laser pulse energy [16–18], and its spatial resolution is high enough. However, this direct-writing method is of low efficiency for the practical manufacturing.

Displacement Talbot Lithography (DTL) is a non-contact photolithographic method. It forms periodic patterns just like proximity printing. The substrate is moving vertically to the mask at a distance corresponding to the Talbot distance of the periodic phase mask. This technique can form a time-integrated image which is of high resolution and contrast [19].

In this work, we fabricated the high-birefringence gratings in Silica-on-Silicon waveguides with DTL. The waveguides were fabricated with i-line lithography, and gratings are etched on the top of the core layer of the waveguides, which leads to the structure with asymmetric refractive-index modulation. The asymmetric geometry and intensive stress induced owing to the surface gratings increase the total birefringence value of waveguides to the value as high as 1.670×10^{-3}. By adjusting the parameters of gratings, we demonstrate the influence of the waveguide width and grating etched depth on birefringence.

2. Experiment process

2.1. Displacement Talbot lithography

The concept of DTL is summarized as Fig. 1(a) shown, the simulation results are obtained by the Finite Element Method (FEM) given by the commercial software COMSOL Multiphysics : first of all, using monochromatic collimated laser beam to illuminate phase-mask can form self-images of the periodic patterns at a Talbot period of approximately $2\Lambda_{mask}{}^2/\lambda_{in}$, where Λ_{mask}=1056.8 nm is the period of phase mask and λ_{in}=377 nm is the wavelength of laser beam. At the same time, it also forms the sub-images at certain distances corresponding to integer fractions of the Talbot period. When the photoresist-coated substrate is moving periodically at constant speed perpendicular to the mask in specific distance H, the combination of self-images and sub-images will be formed in the photoresist at the same time. So that the final Talbot pattern is the integral of the self and sub images. It needs to be pointed out that H should be larger than twice of Talbot length, in this way the period of Talbot pattern will be half of Λ_{mask}, H is three times of Talbot length in our research [19].

According to Ref. [20], when the phase mask is fixed at the XY plane and the photoresist substrate moves periodically at a constant speed along Z direction, the Talbot pattern illuminated by plane wave can use a scalar electric field to demonstrate:

$$\mathrm{Ex,z} = \sum\nolimits_m C_m \exp(imG(x))\exp(ik_m z) \tag{1}$$

where

$$k_m = (k^2 - m^2G^2)^{1/2} \tag{2}$$

In Eq. (2), m is an integer, k=(2π/λ), G=(2π/a), G is the unit reciprocal lattice vector of the phase mask, if the diffraction orders are small enough, the Eq. (2) can be accurate described as follow

$$Z_T(m,n) = 2\pi/(k^2 - m^2G^2)^{1/2} - (k^2 - n^2G^2)^{1/2} \tag{3}$$

where m and n are the different diffraction orders, Z_T is the Talbot length owing to the two chosen orders. In our design, Z_T is 5.925 μm and the 0th order diffraction is suppressed. Figure 1(b) shows the simulation result. According to the single repeated pattern, the scalar electric field energy concentrates in ±1st orders, that is the red rectangles in the center. There are higher diffraction orders remain, multiple orders interaction makes final diffraction image complicated. But the period of Talbot patterns is Λ_{mask}/2, it can form gratings as what we designed [21].

Optical Materials EXPRESS

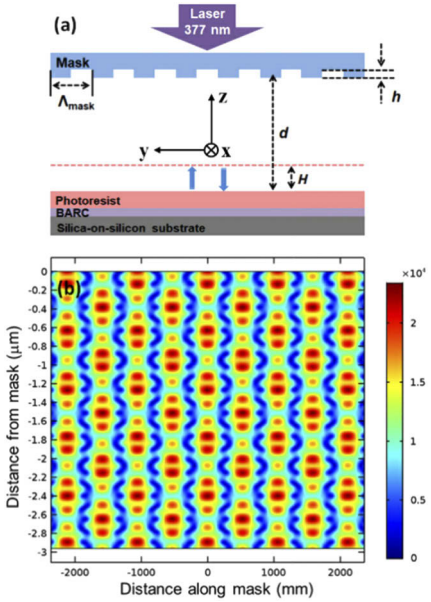

Fig. 1. (a) Schematic diagram of pattern writing with DTL. (b) Simulation result of intensity distribution after the phase mask.

2.2. Device structure and fabrication

Waveguide Bragg grating is fabricated in the Silica-on-Silicon platform, the structure of WBG is shown in Fig. 2(a). It is a typical three-layers rectangle waveguide structure: the upper and lower claddings are both 15 μm SiO_2 layers, the core layer is rectangle waveguide. 30 moles GeO_2 were doped to the core layer to induce 2.5% index difference between the cladding layers, and its thickness is 3.5 μm. The grating was fabricated on the waveguide core layer with DTL. In order to design high birefringence WBG for C-band linear-polarized lasers, coupled-mode and sources of birefringence are adopted as design criteria of the grating. Resonances of forward and reverse transmission caused by WBG satisfy the phase-matching condition [22,23].

$$\beta_1 = \beta_2 + p(2\pi/\Lambda) \text{ or } p\lambda_B = 2n_{eff}\Lambda \tag{4}$$

In which β_1 and β_2 are the propagation constants of the forward and backward guided modes respectively (for opposite directional coupling), Λ is the Bragg grating period, p is the resonance order, λ_B is the Bragg resonance wavelength, and n_{eff} is the effective refractive index of guided mode. In our design, p=1 for the first order grating, Λ is 528.4 nm for the λ_B=1550 nm.

According to Ref. [24], there are two major sources of birefringence. The anisotropic material stress birefringence B_s, when the stress of waveguide in two orthogonal directions is different, the refractive index is different due to photo-elastic effect. The asymmetrical geometrical birefringence B_g, which is the difference of effective refractive index in different directions caused by the asymmetry form. The total birefringence B is given by:

$$B = B_s + B_g \tag{5}$$

Figure 2(b)-(e) show the schematic of the fabrication process, all materials were grown by plasma-enhanced chemical vapor deposition (PECVD). Firstly, a 15 μm silica was grown on the silicon substrate, then the core layer was fabricated with 3.5 μm Ge-doped silica, the materials between the cladding layers and the core layer are different, which will cause anisotropic stress

Optical Materials EXPRESS

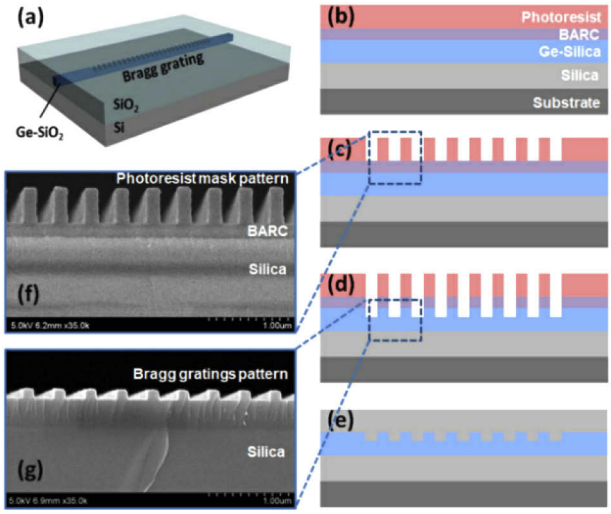

Fig. 2. (a) Schematic diagram of the WBG. (b)~(e) Schematic of the fabrication progress. (f) The SEM of photoresist pattern after DTL. (g) The SEM of Bragg gratings pattern after ICP.

distribution in the surface of waveguide core layer, thus there will be a large value B_s. The bottom anti-reflection coating layer (BARC) was coated on the Silica-on-Silicon substrate, the BARC layer is able to prevent standing wave effect and improve the phase mask quality on photoresist. Then the photoresist with a thickness of 400 nm was coated on BARC layer as shown in Fig. 2(b). The grating pattern was formed in the photoresist with DTL as the Fig. 2(c) shown, the period of selected phase mask Λ_{mask} is 1056.8 nm. The scanning electron microscopy (SEM) image of photoresist mask pattern is shown in Fig. 2(f), the pattern was then etched to the surface of waveguide core layer by Inductively Coupled Plasma (ICP) etching technique. Illustration Fig. 2(g) shows the vertical-section SEM image of Bragg gratings pattern after ICP, the grating duty cycle is 38%, grating period is $\Lambda_{mask}/2 = 528.4$ nm. The side wall steepness of grating grooves is closed to 90°. Then the waveguide was fabricated with i-line lithography. At last, a 15 μm thickness SiO_2 upper cladding was grown.

3. Results and discussion

In order to demonstrate the characteristic of the fabricated WBGs' spectrums and birefringence, the measurement system is built as shown in the Fig. 3, a super-continuous spectrum laser light source (SuperK Compact, NKT Photonics, Inc.) and an optical spectrum analyzer (OSA, AQ6370D, Yokogawa) are used in the measurement, the resolution of the OSA is 0.01 nm. The illustration shows the physical picture of WBG coupled with input/output single mode optical fibers. The refractive index matching fluid is used between the two facets of the optical fibers and the WBG to reduce return loss, its refractive index is 1.4525. The polarization of input light is adjusted by rotating three optical paddles of the polarization controller (PC).

The total birefringence B is calculated from the Bragg resonance wavelength splitting of two orthogonal eigenmodes, the Bragg resonance wavelength λ_B satisfies the above phase-matching condition. The birefringence, which is the effective refractive index difference between TE mode and TM mode $\Delta n_{eff}^{TM-TE} = \Delta n_{eff}^{TM} - \Delta n_{eff}^{TE}$, can be calculated from:

$$\Delta n_{eff}^{TM-TE} = \Delta \lambda_B^{TM-TE} / 2\Lambda \tag{6}$$

Optical Materials EXPRESS

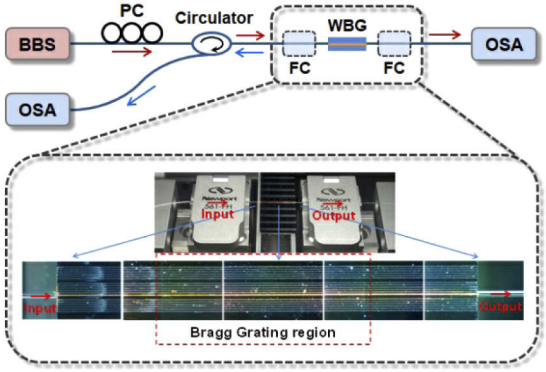

Fig. 3. Schematic diagram of spectrum measurement system, illustration shows the actual system.

where $\Delta\lambda_B^{TM-TE}$ is the separation between the Bragg resonances of TE mode and TM mode. The stress birefringence B_s of waveguides on the Silica-on-Silicon platform is high, which is mainly caused by thermal-expansion mismatch between the silicon substrate and doped core layers. The birefringence can be eliminated by doping material with negative thermal expansion coefficient into core layer. But our design is to fabricate high-birefringence device, GeO_2 has a positive thermal expansion coefficient compare to SiO_2, which induces a high anisotropic stress to the core layer. At the same time, surface etching gratings also induce intensive stress between core layer and up cladding layer, so the B_s of our WBGs is high.

Geometrical birefringence B_g is caused by structure of device. For rectangle waveguide, the main parameters affect B_g are the waveguide width W and height L. if W/L=1, the profile of waveguide is a square and the effective index of TE and TM modes are the same, which means the waveguide has zero-birefringence at this condition. If W/L<1, the structure of waveguide becomes asymmetric and the n_{eff}^{TM} is smaller than n_{eff}^{TE}, so the B_g is negative and vice versa. However, our WBG is fabricated by etching grating on the surface of rectangle waveguide. Meanwhile, grating etched depth has an important influence on the actual effective height of waveguide, therefore affects B_g significantly.

Figure 4(a) shows the transmission (black line) and reflection (blue line) spectrums of the WBG in the state of circular polarization. In circular polarization, the reflectivity of TE mode and TM mode are 58.130% and 57.146% respectively. The waveguide width of WBG in the picture is 3.6 μm and grating etched depth is 121.5 nm. The respective transmission spectrums of TE mode and TM mode in linearly polarization are shown in the Fig. 4(b). The resonance peak in the range from 1540 nm to 1545 nm is ghost mode, which is caused by the coupling between forward core mode and backward low-order cladding modes. The cladding modes attenuate quickly in propagation direction due to the absorption of the claddings, so the ghost mode is kind of strong in transmission spectrum but almost unobservable in reflection [25]. As shown in the Fig. 4(b), the peaks of TE mode and TM mode are 1550.799 nm and 1552.512 nm, the reflectivity of which is 99.927% and 99.928% respectively. The wavelength separation $\Delta\lambda_B$ is 1.7130 nm and the corresponding birefringence is 1.621×10^{-3}. Such a high birefringence value is owing to the different materials' thermal expansion coefficients between the claddings and core layer, resulting in high anisotropic stress in the border region of the layers, thus it leads to high stress birefringence. Meanwhile, the grating etched on the surface of waveguide core layer induces an intensive anisotropic stress. it also changes the geometrical symmetry of the core, because the grating etching changes the effective height of core layer, so that W/L and B_g changes significantly.

Optical Materials EXPRESS

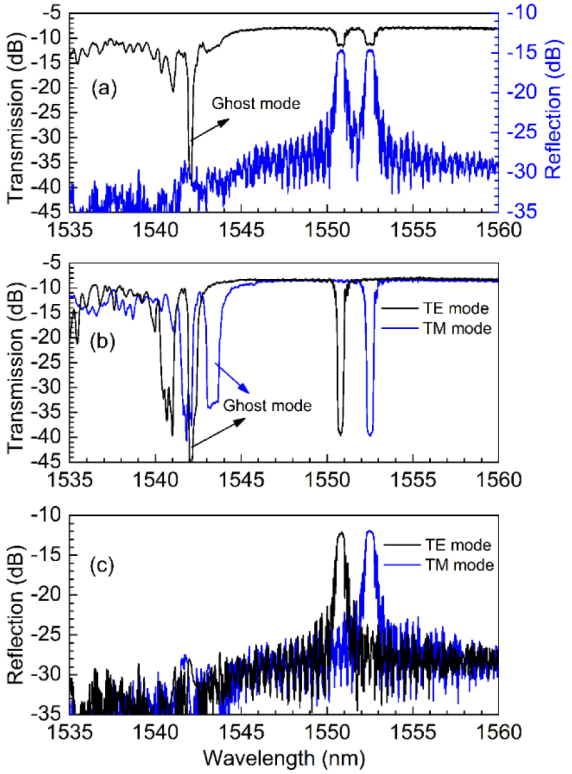

Fig. 4. (a) Transmission (black) and reflection (blue) spectrums of WBG in circular polarization. (b) Transmission spectrums of TE mode (black) and TM mode (blue). (c) Reflection spectrums of TE mode (black) and TM mode (blue).

In order to research the parameters affecting the WBG birefringence, we further analyzed the influence of the waveguide width and grating etched depth on total birefringence B. Figure 5 shows the trends of Bragg resonance wavelength separation and birefringence when the waveguide width increases from 3.3 μm to 3.8 μm. The waveguide height is 3.5 μm and grating etched depth is 121.3 nm. All the data points are the average of multiple measurements to reduce measurement errors, such as vibration of test bench and the position of PC's paddles. Because the grating etched depth of waveguides is the same, the actual effective height of waveguides can be assumed as a constant. In this condition, only the waveguide width W could change the geometrical shape of the waveguide core perpendicular to the direction of light propagation. It can be seen that the birefringence decreases with the width in the range of 3.3 μm to 3.6 μm, the birefringence decreases from 1.670×10^{-3} to 1.621×10^{-3}. As we discussed above, the initial W/L<1, which means there is a negative geometrical birefringence B_g in this range [26]. With increasing of waveguide width, the geometrical asymmetry in the two orthogonal directions decreases and the negative birefringence decreases, thus the total birefringence decreases. The minimum value of birefringence is at 3.6 μm rather than 3.5 μm in theory. This is owing to the fabrication errors during material growth, lithography and grating etching, which result in the effective height of WBG is 3.6 μm. With the further increasing of waveguide width, W/L>1 and the geometrical birefringence B_g becomes positive. The increase of W will make the shape of waveguide grating more asymmetric in two orthogonal directions, so the WBG birefringence increase with the width. The highest WBG birefringence reaches 1.670×10^{-3}. To our knowledge, it is the highest birefringence value of the rectangle waveguide Bragg grating in Silica-on-Silicon platform.

Optical Materials EXPRESS

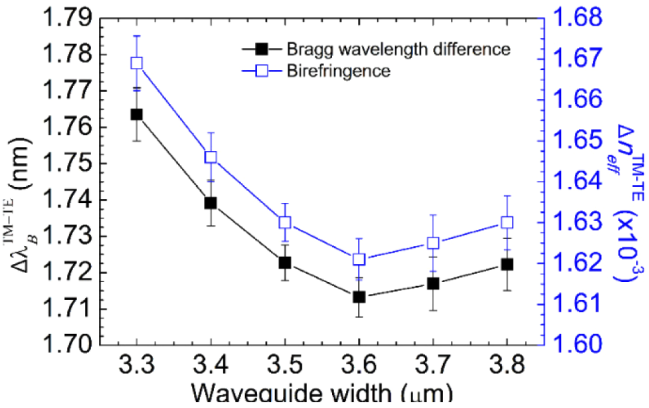

Fig. 5. The trend of birefringence(blue) and Bragg wavelength difference (black) changing with waveguide width W, Error bar is the averaged multiple times.

Figure 6 shows the influence of grating etched depth on WBG Bragg wavelength separation and birefringence. the waveguide width and the grating period is 3.6 μm and 528.4nm respectively. The WBG birefringence is positively correlated with etching depth. When the etching depth of grating increases from 92.5 nm to 121.3 nm, the birefringence increases from 7.919×10^{-4} to the highest value. There are two main reasons for the increase of birefringence [27]. Firstly, the grating etched depth can directly change the effective height of WBG. The W/L increase with the grating etched depth, the B_g also increase with it too. Another reason is the etched grating may induce dense stress on the surface of waveguide core, in addition the SiO_2 was grown after grating etching. As the etching depth increasing, the anisotropic stress between etched and non-etched regions (grating region) increases greatly due to the thermal expansion mismatch.

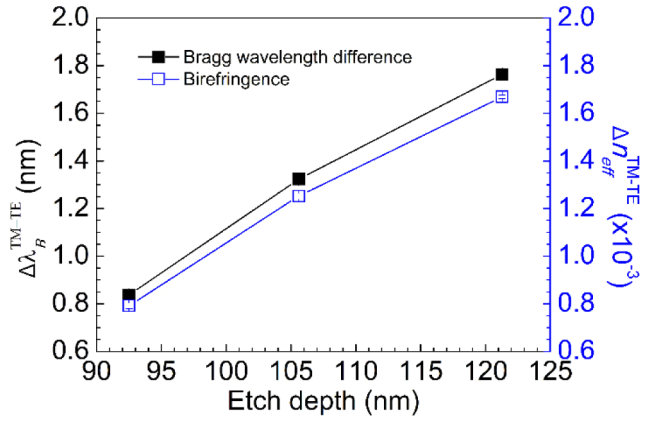

Fig. 6. Influence of grating etched depth on WBG Bragg wavelength separation and birefringence

4. Conclusion

In conclusion, we have designed a rectangle waveguide with surface etched Bragg gratings and fabricated it with PECVD and DTL in the Silica-on-Silicon platform. Based on the high-stress birefringence of Silica-on-Silicon platform, the birefringence of WBG is controllable though adjusting waveguide width and grating etched depth. Compare to WBGs in other platforms, the

Optical Materials EXPRESS

device here has a mode splitting as large as 1.7635 nm between TE mode and TM mode. It is endowed with excellent wavelength-selective and polarization-mode selective functions. This WBG can be used to construct linear-polarization external semiconductor lasers with improved PER performance, showing promising potential applications in polarization-dependent optical communication and sensing systems.

Funding

National Key Research and Development Program of China (2016YFE0126800); National Natural Science Foundation of China (61874119, 61674148, 61727822, 51672264); Science and Technology Development Project of Jilin Province (20180201014GX).

Disclosures

The authors declare that there are no conflicts of interest related to this article.

References

1. D. Dai, J. Bauters, and J. E. Bowers, "Passive technologies for future large-scale photonic integrated circuits on silicon: polarization handling, light non-reciprocity and loss reduction," Light: Sci. Appl. **1**(3), e1 (2012).
2. M. Lobino and J. O'Brien, "Entangled photons on a chip," Nature **469**(7328), 43–44 (2011).
3. L. A. Fernandes, J. R. Grenier, P. R. Herman, J. S. Aitchison, and P. V. S. Marques, "Stress induced birefringence tuning in femtosecond laser fabricated waveguides in fused silica," Opt. Express **20**(22), 24103–24114 (2012).
4. J. Wang, L. C. Guan, C. Chen, R. Cheng, C. Wang, X. Sun, Y. Wu, and D. Zhang, "Metal-print-defining thermo-optic tunable chirped waveguide Bragg gratings using organic-inorganic hybrid PMMA materials," Opt. Mater. Express **8**(7), 1870–1881 (2018).
5. R. K. Kim, J. H. Song, Y. Oh, D. Jang, J. R. Kim, and K. S. Lee, "Circularly polarized external cavity laser hybrid integrated with a polyimide quarter-wave plate on Planar Lightwave Circuit," IEEE Photonics Technol. Lett. **19**(14), 1048–1050 (2007).
6. R. K. Kim, J. H. Lim, J. H. Song, and K. S. Lee, "Highly linear-polarized external cavity lasers hybrid integrated on planar lightwave circuit platform," IEEE Photonics Technol. Lett. **18**(4), 580–582 (2006).
7. Z. Wang, K. V. Gasse, V. Moskalenko, S. Latkowski, E. Bente, B. Kuyken, and G. Roelkens, "A III-V-on-Si ultra-dense comb laser," Light: Sci. Appl. **6**(5), e16260 (2017).
8. M. Burla, L. R. Cortés, M. Li, X. Wang, L. Chrostowski, and J. Azãna, "Integrated waveguide Bragg gratings for microwave photonics signal processing," Opt. Express **21**(21), 25120–25147 (2013).
9. A. P. Bakoz, A. A. Liles, A. A. Gonzalez-Fernandez, T. Habruseva, C. Hu, E. A. Viktorov, S. P. Hegarty, and L. O'Faolain, "Wavelength stability in a hybrid photonic crystal laser through controlled nonlinear absorptive heating in the reflector," Light: Sci. Appl. **7**(1), 39 (2018).
10. B. Tabti, F. Nabki, and M. Ménard, "Polarization insensitive Bragg gratings in Si_3N_4 waveguides," in *Advanced Photonics Congress*, (2017), pp IW2A.5.
11. N. Son, K. Kim, J. Kim, and M. Oh, "Near-infrared tunable lasers with polymer waveguide Bragg gratings," Opt. Express **20**(2), 827–834 (2012).
12. S. Yliniemi, J. Albert, Q. Wang, and S. Honkanen, "UV-exposed Bragg gratings for laser applications in silver-sodium ion-exchanged phosphate glass waveguides," Opt. Express **14**(7), 2898–2903 (2006).
13. H. Yun, Z. Chen, Y. Wang, J. Fluekiger, M. Caverley, L. Chrostowski, and N. Jaeger, "Polarization-rotating, Bragg-grating filters on silicon-on-insulator strip waveguides using asymmetric periodic corner corrugations," Opt. Lett. **40**(23), 5578–5581 (2015).
14. M. Shokooh-Saremi, V. G. Ta'eed, N. J. Baker, I. C. M. Littler, D. J. Moss, B. J. Eggleton, Y. Ruan, and B. Luther-Davies, "High-performance Bragg gratings in chalcogenide rib waveguides written with a modified Sagnac interferometer," J. Opt. Soc. Am. B **23**(7), 1323–1331 (2006).
15. D. T. Spencer, M. Davenport, S. Srinivasan, J. Khurgin, P. A. Morton, and J. E. Bowers, "Low kappa, narrow bandwidth Si_3N_4 Bragg gratings," Opt. Express **23**(23), 30329–30336 (2015).
16. H. Zhang, S. M. Eaton, and P. R. Herman, "Single-step writing of Bragg grating waveguides in fused silica with an externally modulated femtosecond fiber laser," Opt. Lett. **32**(17), 2559–2561 (2007).
17. Q. Guo, Y. Yu, Z. Zheng, C. Chen, P. Wang, Z. Tian, Y. Zhao, X. Ming, Q. Chen, H. Yang, and H. Sun, "Femtosecond laser inscribed sapphire fiber Bragg grating for high temperature and strain sensing," IEEE Trans. Nanotechnol. **18**, 208–211 (2019).
18. C. Chen, X. Zhang, Y. Yu, W. Wei, Q. Guo, L. Qin, Y. Ning, L. Wang, and H. Sun, "Femtosecond laser-inscribed high-order Bragg gratings in large-diameter sapphire fibers for high-temperature and strain sensing," J. Lightwave Technol. **36**(16), 3302–3308 (2018).
19. H. H. Solak, C. Dais, and F. Clube, "Displacement Talbot lithography: a new method for high-resolution patterning of large areas," Opt. Express **19**(11), 10686–10691 (2011).

Optical Materials EXPRESS

20. J. D. Mills, C. W. J. Hillman, B. H. Blott, and W. S. Brocklesby, "Imaging of free-space interference patterns used to manufacture fiber Bragg gratings," Appl. Opt. **39**(33), 6128–6135 (2000).
21. C. W. Smelser, S. J. Mihailov, D. Grobnic, P. Lu, R. B. Walker, H. Ding, and X. Dai, "Multiple-beam interference patterns in optical fiber generated with ultrafast pulses and a phase mask," Opt. Lett. **29**(13), 1458–1460 (2004).
22. T. Erdogan, "Fiber grating spectra," J. Lightwave Technol. **15**(8), 1277–1294 (1997).
23. C. Chen, Y. Yu, R. Yang, C. Wang, J. Guo, Y. Xue, Q. Chen, and H. Sun, "Reflective optical fiber sensors based on tilted fiber Bragg gratings fabricated with femtosecond laser," J. Lightwave Technol. **31**(3), 455–460 (2013).
24. X. Dai, S. J. Mihailov, C. L. Callender, R. B. Walker, C. Blanchetière, and J. Jiang, "Birefringence control and dimension monitoring of silica-based ridge waveguides using Bragg gratings and ultraviolet irradiation," Opt. Eng. **44**(12), 124062 (2005).
25. T. Erdogan and J. Sipe, "Tilted fiber phase gratings," J. Opt. Soc. Am. A **13**(2), 296–313 (1996).
26. M. F. Hossain, H. P. Chan, and A. Z. Kouzani, "Efficient design of polarization insensitive polymer optical waveguide devices considering stress-induced effects," Opt. Express **22**(8), 9334–9343 (2014).
27. I. Richter, P. Sun, F. Xu, and Y. Fainman, "Design considerations of form birefringent microstructures," Appl. Opt. **34**(14), 2421–2429 (1995).